JBC RESEARCH ARTICLE

Intrinsically disordered plant protein PARCL colocalizes with RNA in phase-separated condensates whose formation can be regulated by mutating the PLD

Received for publication, May 20, 2022, and in revised form, October 16, 2022 Published, Papers in Press, October 21, 2022,
https://doi.org/10.1016/j.jbc.2022.102631

Anna Ostendorp[1,*,‡], Steffen Ostendorp[1,‡], Yuan Zhou[2], Zoé Chaudron[1], Lukas Wolffram[1], Khadija Rombi[1], Linn von Pein[1], Sven Falke[3,4], Cy M. Jeffries[5], Dmitri I. Svergun[5], Christian Betzel[3,4], Richard J. Morris[6], Friedrich Kragler[2], and Julia Kehr[1]

From the [1]Universität Hamburg, Department of Biology, Institute of Plant Science and Microbiology, Hamburg, Germany; [2]Max Planck Institute of Molecular Plant Physiology, Department II, Potsdam, Germany; [3]Laboratory for Structural Biology of Infection and Inflammation, c/o DESY, Hamburg, Germany; [4]Universität Hamburg, Department of Chemistry, Institute of Biochemistry and Molecular Biology, Hamburg, Germany; [5]European Molecular Biology Laboratory (EMBL) Hamburg Site, c/o DESY, Hamburg, Germany; [6]Computational and Systems Biology, John Innes Centre, Norwich, United Kingdom

Edited by Wolfgang Peti

In higher plants, long-distance RNA transport *via* the phloem is crucial for communication between distant plant tissues to align development with stress responses and reproduction. Several recent studies suggest that specific RNAs are among the potential long-distance information transmitters. However, it is yet not well understood how these RNAs enter the phloem stream, how they are transported, and how they are released at their destination. It was proposed that phloem RNA-binding proteins facilitate RNA translocation. In the present study, we characterized two orthologs of the phloem-associated RNA chaperone-like (PARCL) protein from *Arabidopsis thaliana* and *Brassica napus* at functional and structural levels. Microscale thermophoresis showed that these phloem-abundant proteins can bind a broad spectrum of RNAs and show RNA chaperone activity in FRET-based *in vitro* assays. Our SAXS experiments revealed a high degree of disorder, typical for RNA-binding proteins. In agroinfiltrated tobacco plants, eYFP-PARCL proteins mainly accumulated in nuclei and nucleoli and formed cytosolic and nuclear condensates. We found that formation of these condensates was impaired by tyrosine-to-glutamate mutations in the predicted prion-like domain (PLD), while C-terminal serine-to-glutamate mutations did not affect condensation but reduced RNA binding and chaperone activity. Furthermore, our *in vitro* experiments confirmed phase separation of PARCL and colocalization of RNA with the condensates, while mutation as well as phosphorylation of the PLD reduced phase separation. Together, our results suggest that RNA binding and condensate formation of PARCL can be regulated independently by modification of the C-terminus and/or the PLD.

The vascular system of higher plants enables the translocation of nutrients and signaling molecules and has therefore been termed an information superhighway (1). Phloem transported macromolecules, such as RNAs and proteins, are thought to be among the important information transducers (2–7). Analyses of phloem samples identified different RNA species, including ribosomal RNAs, messenger RNAs (mRNAs), and small noncoding RNAs like transfer RNAs (tRNAs), tRNA and ribosomal RNA fragments, miRNAs, and siRNAs (8–12). In addition, grafting experiments demonstrated that RNAs can be translocated from shoot to root and vice versa (6, 13). However, there are only few cases where a signaling function of mobile RNAs could be demonstrated. Specific miRNAs were found to be accumulated in the phloem under nutrient deficiency and can move over long distances to regulate nutrient allocation (2, 3, 7, 14). Also, mobile FLOWERING LOCUS T (*FT*) mRNA has been suggested to contribute to the systemic regulation of floral induction (15), in addition to the major regulator FT protein (16, 17). Similarly, phloem-transported mRNAs encoding TRANSLATIONALLY CONTROLLED TUMOR PROTEIN 1 (*TCTP1*) and homeodomain transcription factors induce tuber formation in potato and root formation in Arabidopsis, respectively (6, 18–20).

It is well accepted that RNAs are accompanied by RNA-binding proteins (RBPs) and are transported as ribonucleoprotein (RNP) complexes within a cell or between different cells, tissues, and organs. Accordingly, large protein and RNP complexes have been observed in phloem samples, indicating that RBPs are also essential for RNA long-distance transport (21–23). It has been suggested that RNA secondary structures and/or base modifications, that could affect the interaction with RBPs, can promote phloem mobility (24, 25).

It was estimated that the proteome of any organism contains 3 to 11% RBPs (26). The interaction of RNAs with RBPs helps to establish and/or maintain the native secondary structure of RNAs, thus enabling a correct function or localization of RNA molecules. RNA–protein interactions also increase RNA

‡ The authors wish it to be known that, in their opinion, the first 2 authors should be regarded as joint co-first authors.
* For correspondence: Anna Ostendorp, anna.ostendorp@uni-hamburg.de.

stability by protecting them against nucleases and oxidizing agents (27–29). Many RBPs possess specific RNA-binding domains, including predictable RNA recognition motifs, K-homology domains, double-stranded RNA-binding domains, zinc finger domains, glycine- and arginine-rich regions, and others (26, 30). RBPs are typically classified based on known RNA-binding domains. However, also proteins lacking predictable RNA-binding domains can have nucleic acid binding capacity, such as the highly conserved HSC70 chaperones (31).

RBPs are often at least partially disordered, therefore belonging to the intrinsically disordered proteins (IDPs). Interestingly, ∼20% of mammalian RBPs show intrinsic disorder in over 80% of their sequence, allowing protein–protein and protein–RNA interactions (32). These interactions can be modulated by posttranslational protein modifications like phosphorylation or acetylation. Especially phosphorylation of disordered RBPs can change affinity and specificity toward RNAs or interacting proteins significantly (26, 33). One group of RBPs with a high degree of disorder are RNA chaperones and RNA remodeling proteins. RNA chaperones are defined as RBPs transiently binding RNAs and facilitating correct folding by stabilizing or destabilizing secondary structures. RNA chaperones play many pivotal roles affecting growth, stress tolerance, and virulence in plants and bacteria (34–36).

Several RBPs contain a prion-like domain (PLD), a typical motif found in IDPs (37, 38). The PLD itself does not bind RNA, but approximately 12% of PLD-containing proteins show RNA-binding properties (38). Typically, RBPs harboring a PLD tend to form cellular condensates by liquid-liquid phase transition without losing functionality. They are also known to build large granules consisting of different RBPs and RNAs that can regulate translation, translocation, and mRNA stability (39–42). Recently, approximately, 500 PLD-containing proteins were predicted computationally in the model plant *Arabidopsis thaliana* (43), but as yet, only a few prion-like plant proteins have been studied in more detail (43–48).

The phloem proteome encompasses many RBPs with well-known RNA-binding domains, such as ribosomal proteins and translation initiation and elongation factors (49–51). Also, glycine-rich RBPs have been identified and may play a role in RNA transport in the phloem (9, 50). Other phloem RBPs have not yet been characterized and have no annotated functions (49, 50, 52). In the present study, we functionally and structurally analyzed two orthologs of a formerly uncharacterized phloem protein that we, due to its characteristics, named phloem-associated RNA chaperone-like protein (PARCL). PARCL proteins are small (<20 kDa), plant-specific proteins harboring a predicted PLD. Our results show that PARCL proteins are phloem-abundant, highly disordered RBPs with RNA chaperone activity that can form large condensates within cells. Phase separation seems to be linked directly to the PLD, as tyrosine to glutamate mutations within the PLD strongly reduced their formation. This was confirmed by phase separation experiments *in vitro* that also showed that if RNA is added, it is incorporated into the condensates and that mutation as well as phosphorylation of the PLD inhibits phase separation.

Results

PARCL identification and in silico *characterization*

PARCL is a highly abundant phloem protein that was initially identified by MS as a homolog of the uncharacterized *Arabidopsis* protein At1g64370 after 2D electrophoresis from *Brassica napus* phloem proteins (50). To enrich positively charged proteins including nucleic acid–binding proteins, we subjected native phloem exudate from *B. napus* to heparin affinity chromatography (53–55). Phloem proteins eluting at NaCl concentrations higher than 1.5 M were separated by 1D SDS-PAGE revealing 13 well-defined protein bands (Fig. 1*A*). MALDI-TOF MS analysis identified PARCL as the most abundant protein (Fig. 1*A* and Table S1). The PARCL bands showed a strong signal after phosphoprotein staining, indicating the presence of several phosphorylation sites. *In silico* analyses revealed that PARCL proteins are highly conserved basic proteins (pI > 9.5) (Fig. S1 and Table S2) in Brassica species that do not harbor common RNA-binding domains but possess distinct motifs enabling protein:protein and protein:nucleic acid interactions. The N-terminal region contains a highly repetitive amino acid patch with the motif GYGSQS, showing strong similarity to PLDs present in many RBPs (37). Furthermore, a KR basic patch at the C-terminus followed by an S-rich region is predicted by Pprint to enable nucleic acid interactions (Fig. 1*B*). The S-rich region is a predicted phosphorylation site for CKII-like kinases with at least six to seven potential phosphorylations. The occurrence of such a region is in good accordance with the observed intense signal after phosphoprotein staining (Fig. 1*A*). Additionally, an N-terminal acetylation site was identified by MS (Fig. S2).

RNA-binding activity

The strong binding of heparin and the predictions by Pprint suggested that PARCL proteins can bind RNA (Fig. 1*B*). To verify this, different long and short RNAs and DNAs were used for *in vitro* Microscale thermophoresis (MST) assays: the phloem-abundant 21 nucleotide long miRNAs 398, 164, and 396 (2, 3) as RNA and complementary DNA, full-length folded transfer $tRNA_{Met}$, *PARCL* mRNA, and a 21-nucleotide long RNA probe (21R-) that does not form any secondary structures was used to confirm RNA chaperone activity (56, 57). *PARCL* mRNA was chosen, since the transcript was found in *B. napus* phloem sap (Fig. 2*A*). While the dissociation constants (Kd) for RNAs were in the low μM range, the Kd for DNA could not be determined (>500 μM), showing that PARCL has a strong preference for RNA (Fig. S3*A* and Table S3). PARCL showed similar binding affinities towards phloem RNAs of different lengths (miRNAs, tRNA, mRNA), with equilibrium dissociation constants (Kd) ranging between 1.3 and 2.9 μM (Fig. 2*B* and Table S3). Sense and antisense miR164 were bound with similar affinity (1.71 μM and 1.73 μM). Significantly, lower affinities were observed for 21R- RNAs, irrespective if single- or double stranded. To exclude that the stronger binding to the other RNAs was caused by the additional bases introduced by *in vitro* transcription, three guanines were added to the 21R-probe at its 5′ end (21Rmod). The affinity even decreased

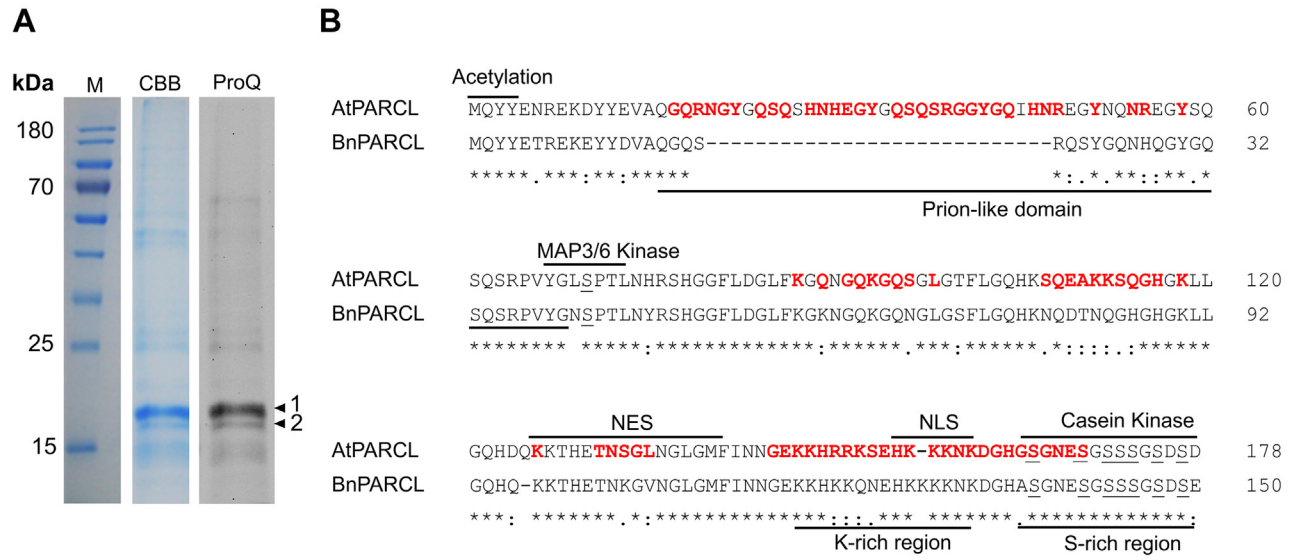

Figure 1. Identification of PARCL protein from *Brassica napus* phloem sap and bioinformatic analysis of existing motifs and domains. *A*, for the identification of RNA-binding proteins, heparin affinity chromatography with native *Brassica napus* phloem exudate was performed. Proteins were eluted with increasing NaCl concentrations and finally separated by SDS-PAGE. After staining with colloidal Coomassie (CBB), two abundant protein bands appeared at high salt concentrations (1 and 2). Phosphoprotein staining by Pro-Q Diamond Phosphoprotein Gel Stain (ProQ) revealed that both bands harbor highly phosphorylated proteins. Mass spectrometric analyses revealed that both bands contained the same protein (PARCL, Acc. No. CDY46524) but obviously with a different phosphorylation state. *B*, secondary modifications and RNA-binding of PARCL. Using selected prediction algorithms for possible modification sites and binding motifs, several sites within the PARCL sequences from *Brassica napus* and the homolog from *Arabidopsis thaliana* could be identified including N-terminal acetylation, MAP3/6 kinase phosphorylation, and CKII phosphorylation sites. Furthermore, a predicted NLS and NES are present as well as a probable prion-like domain at the N-terminus. Predicted RNA-binding sites are represented as *red bold* letters. PARCL, phloem-associated RNA chaperone-like.

from 15 μM to 28 μM (Fig. 2*B* and Table S3), suggesting that the additional G bases are not responsible for the higher affinity to PARCL. The measurements with the 21R- RNA that lacks secondary structures (56, 57), single- and double-stranded miR164, and tRNA indicated that dsRNA regions are probably not relevant for the PARCL–RNA interaction (Fig. 2*B* and Table S3). As mentioned above, PARCL proteins are highly similar within different Brassica species, the main difference between orthologs being the length of the PLD (Figs. 1*B*, S1*C* and S4). Compared to *A. thaliana* PARCL (AtPARCL), *B. napus* (BnPARCL) has a twenty amino acid shorter PLD. To address whether the PLD variance resulted in different RNA-binding activities, we compared the affinity of both proteins to $tRNA_{Met}$. As shown in Fig. S3*B*, both orthologs having PLD regions of different lengths exhibited almost identical tRNA-binding affinities. For other PLD-containing proteins like FUS or hnRNPA2, it has been shown that PLDs can be phosphorylated what adds additional negative charges

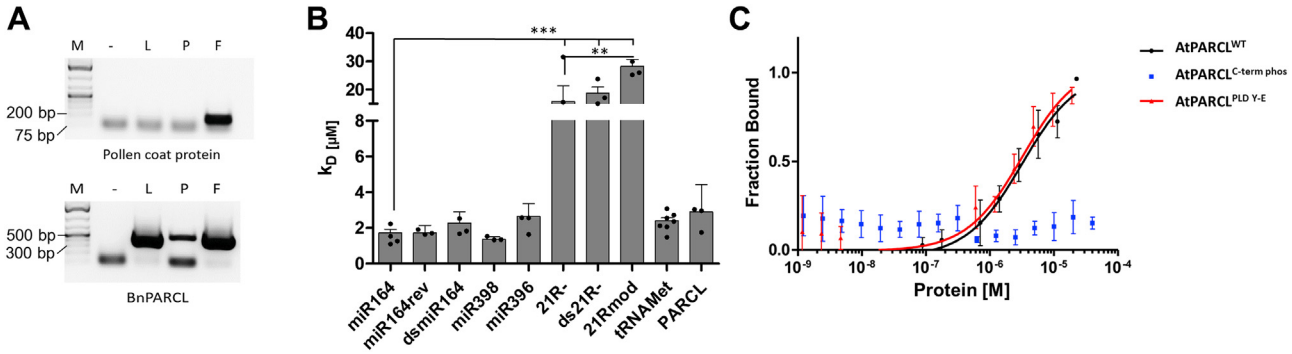

Figure 2. PARCL RNA binding and effects of protein phosphorylation on RNA affinities. *A*, PARCL mRNA tissue localization. To test the phloem localization of the PARCL transcript, phloem RNA was extracted and RT-PCR amplified. The transcript of the pollen coat protein served as a control for pure phloem sap. The PARCL transcript was observable in all tested tissues (leaf (L), phloem (P), and flower (F), whereas the pollen coat protein mRNA was only present in flowers. *B*, RNA dissociation constants detected by MST. Various short and long RNAs were used to identify common RNA-binding preferences. Error bars represent SD from n > 3 repeated measurements; individual measurements are depicted as scatter plots. One-way ANOVA with either miR164 or 21Rmod as control was used for statistical analyses. Binding differences with $p < 0.05$ were regarded as significant (**$p < 0.01$; ***$p < 0.0001$). *C*, difference in RNA binding of unphosphorylated and phosphorylated AtPARCL against labeled miR164 as measured by MST. Addition of multiple negative charges within the PLD ($PARCL^{PLD\ Y\text{-}E}$) did not affect RNA-binding affinities, whereas a C-terminal hyperphosphorylation led to an entire loss of RNA binding within the measured concentration range. MST, Microscale thermophoresis; mRNA, messenger RNA; PARCL, phloem-associated RNA chaperone-like; PLD, prion-like domain.

to this region (58, 59). To determine if changing the net charge of the PLD affects RNA affinity, tyrosines in the AtPARCL PLD were replaced by glutamates what is often used to mimic protein phosphorylation. These mutations did not interfere with RNA binding (Fig. 2*C*). However, phosphorylation of PARCL by CKII at the predicted phosphorylation site at the S-rich C terminus (Fig. 1*B*) that was confirmed by mutating the S-segment serine to alanine residues ($PARCL^{C\text{-}term\ S\text{-}A}$, Fig. S5) strongly reduced RNA-binding activity (Fig. 2*C*). These observations suggest that the C-terminus and not the PLD domain is involved in protein:RNA interactions.

Chaperone activity

RNA chaperone activity assays of PARCL proteins using 21R+ and 21R- RNAs were performed as described previously (56, 57). These RNAs were chosen, because they occur without any secondary structures and therefore annealing activity can be observed by a FRET signal increase over time (56, 57). The assays revealed a similar annealing activity for both RNAs with a K_{ann} of 0.005 s^{-1}, but strand displacement could not be detected (Fig. 3*A*). In contrast to RNA alone (K_{ann} = 0.0051 s^{-1}), PARCL increased the 21R+ and 21R- RNA annealing activity about 4-fold (K_{ann} = 0.019 s^{-1}), a similar activity as measured with StpA that is known to facilitate RNA strand displacement and annealing (56, 57). The annealing activity was concentration dependent and decreased with RNA protein ratios lower than 1:100. Larger ratios led to a saturating effect with a K_{ann} up to 0.02 s^{-1} (Fig. 3*B*). Additionally, higher activity could be observed at lower pH peaking at pH 6 (Fig. S6*B*), whereas chaperone activity decreased with increasing salt concentration and was lost at NaCl concentrations higher than 500 mM (Fig. 3*C*). Like in the MST measurements, phosphorylating PARCL at its C-terminus stopped any annealing activity (Fig. S6*D*). In contrast, heat denaturation of PARCL did not influence RNA annealing rates, indicating a high degree of disorder (Fig. S6*C*).

Structural analysis

We applied small angle X-ray scattering (SAXS) to further evaluate the structural parameters and the in-solution state of PARCL at pH 6.5 and 7.5 (Figs. 3, *D*, *E* and S7), while multi-angle laser light scattering and quasi-elastic light scattering were used to validate the molecular weight and obtain the hydrodynamic radius of the protein (Table S4). PARCL appeared monomeric at both pH values as assessed directly from the SAXS profiles (22–28 kDa) and the multi-angle laser light scattering data (20 kDa; Fig. S8*A*). A comparison of the SAXS data (Fig. S8) and the structural parameters R_g,

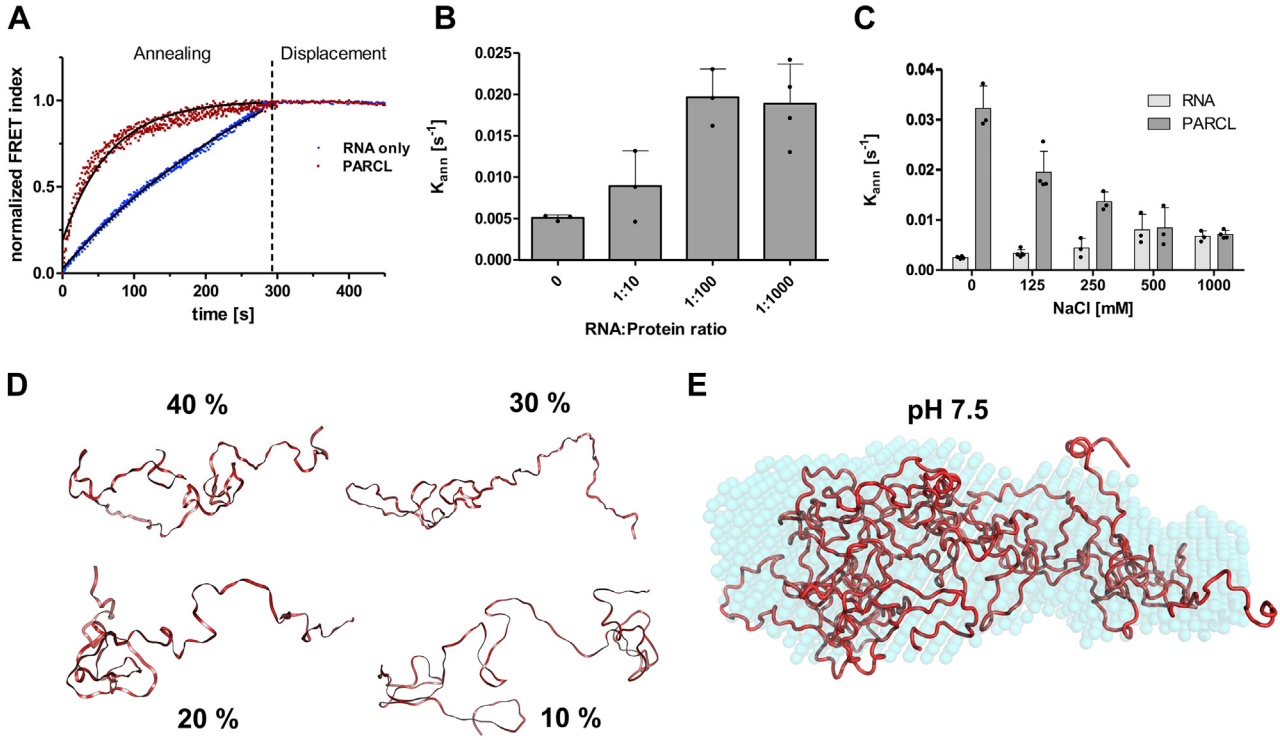

Figure 3. RNA chaperone effects and solution structure of AtPARCL. *A*, difference in RNA annealing between RNA only (*blue*) and with additional 1 μM PARCL (*red*). Annealing could be observed due to an increase of the FRET signal. Strand displacement by an unlabeled complementary RNA strand did not induce a loss of the FRET signal indicating no exchange of the labeled and unlabeled strand. *B*, PARCL concentration-dependent annealing activity. With increasing protein concentrations, the overall annealing rate increased up to 0.02 s^{-1}. Scatter plots resemble single measurements n > 3. *C*, RNA annealing with increasing salt concentrations. The RNA annealing rate in the presence of PARCL decreased with increasing salt concentration, whereas the RNA annealing without PARCL increased until both showed the same velocity at 1000 mM NaCl. Single measurements are highlighted as scatter plots; measurements were performed in at least triplicates (n > 3). *D*, volume-fraction weighted estimates of the model representatives describing the final EOM-refined PARCL ensembles. *E*, spatially aligned ensemble model representatives of PARCL at pH 7.5 (*ribbons*) superposed with the anisotropic 'shape volume' of the ensemble obtained from dummy atom modeling (*transparent spheres*). Error bars represent SDs from repeated measurements. EOM, ensemble optimization method; PARCL, phloem-associated RNA chaperone-like.

maximum dimension, D_{max}, and Porod volume (Table S4) showed only minor differences caused by a change in pH (for example, in R_g, pH 7.5 = 3.7 nm; pH 6.5 = 3.9 nm). Consistent with the CD spectra, the R_g/R_h ratio of 1.2 to 1.3 (compared to a compact protein ratio of 0.8) and subsequent dimensionless Kratky plot (Fig. S7*A*) demonstrate that PARCL is an IDP. The purified AtPARCL and BnPARCL proteins were further subjected to CD measurements including diverse potential ligands like divalent ions, tRNA, and detergents for an initial structural characterization. The measurements showed that both proteins are highly unstructured with no detectable β-sheets and an α-helix content below 5% (Table 1 and Fig. S9). Although approximately 19% shorter than the Arabidopsis protein, BnPARCL showed the same level of disorder. Addition of tRNA had no effect on secondary structure (Table 1).

Since many RBPs need divalent metal ions for their interaction with RNA (30, 60, 61), we performed metal affinity chromatography experiments indicating that PARCL binds Zn^{2+}, Ni^{2+}, Cu^{2+}, and Co^{2+}, but not Mg^{2+}, Ca^{2+}, Fe^{3+}, or Cd^{2+} (Fig. S10). However, except Zn which had a minimal effect on β-sheets, the addition of these metal ions did not alter protein structure in CD experiments (Table 1 and Fig. S9). Noteworthy, the ionic detergent SDS had a significant effect on protein structure. Already a molar protein:SDS ratio of 1:100 induced an increase of α-helices from 5% to 20% and a gain of β-sheet structure from 0% to 11%. Further increasing the molar excess of SDS led to additional α-helical structures, while β-sheets remained almost constant (Table 1 and Fig. S9). Addition of 10 mM SDS shifted the conformation from an entirely disordered to a predominantly ordered structure. The nonionic detergent Tween-20 did not induce any conformational rearrangements.

PARCL localization and phase separation

To analyze the subcellular localization of PARCL and the effect of mutations in the PLD or the C-terminus, N-terminally eYFP-tagged fusion constructs of PARCL were transiently expressed in *Nicotiana benthamiana*, and leaves were examined by confocal microscopy. In most cells, the eYFP-wildtype PARCL fusion ($PARCL^{WT}$) appeared as condensates in the cytosol, in nuclei and nucleoli (Fig. 4, *A* and *B*). As known for several other PLD-containing proteins like Fus, phosphorylation within the PLD can regulate condensate formation (58, 59), no matter if S/T or Y are phosphorylated. Therefore, we mutated Y to E at amino acid positions 22, 33, 42, 51, and 58 in the central PLD motif GYGSG ($PARCL^{PLD\ Y\text{-}E}$) to change the net charge similar to a phosphorylation and examined the effect on condensation. Interestingly, after transient expression of $PARCL^{PLD\ Y\text{-}E}$, much less condensates were detected, and the mutant protein appeared less abundant in nuclei and nucleoli (Fig. 4*B*). A PARCL mutant where S was exchanged against E at positions 169, 171 to 173, 175 and 177 in the C-terminus ($PARCL^{C\text{-}term\ S\text{-}E}$) to mimic phosphorylation of the C-terminus preserved condensates, but nucleolar localization was slightly weaker (Fig. 4, *B* and *C*). To further validate the phase separation properties of PARCL, *in vitro* assays were performed. Here, phase separation could be induced under physiological conditions in 10% PEG 3350 and low salt regime (<150 mM NaCl) at neutral pH (Fig. 5). Condensates started to emerge at PARCL concentrations higher than 1 μM (Fig. 5*A*). Higher protein concentrations first increased the number of condensates and at concentrations above 6 μM, their size increased (Fig. 5*A*). Since PARCL can bind RNAs (Fig. 2*B* and Table S3), RNA was added to the phase separation assays to see if it ends up in the condensates. Cy3-labeled small RNA colocalized with the phase separated protein (Fig. 5*B*), as has been shown for other phase separating RBPs (62–65). The appearance of condensate changed upon addition of RNA, depending on RNA concentration and RNA:protein ratio, the size of droplets decreasing at lower ratios (Fig. 5*C*). In contrast to unphosphorylated $PARCL^{WT}$, $PARCL^{PLD\ Y\text{-}E}$ and $PARCL^{WT}$ phosphorylated by the tyrosine kinase FES (Fig. S11 and Table S6) showed an obvious decrease in condensate number at 10 μM concentration (Fig. 5*D*).

Table 1
Changes in secondary structures of PARCL upon addition of different ligands and additives

Additive	α-helical	β-sheet	Random
$PARCL_{Phos}$	5%	0%	95%
PARCL	5%	0%	95%
+ SDS			
0.5 mM	21%	11%	68%
5 mM	38%	6%	56%
10 mM	44%	12%	44%
+ Tween-20	5%	0%	95%
+ tRNA	6%	0%	94%
+ Fe^{3+}	9%	0%	91%
+ Mg^{2+}	7%	0%	93%
+ Ni^{2+}	5%	0%	95%
+ Zn^{2+}	7%	7%	86%

Discussion

Recent plant phloem studies have found various RNAs in the long-distance transport system including miRNAs, mRNAs, tRNAs and fragments thereof, and ribosomal RNAs. Additionally, all studied phloem proteomes contain many RBPs with distinct RNA-binding domains, and even large ribonuclear complexes have been found (22, 23). However, many phloem proteins have no known function or predicted domain architecture. Here, we characterized one of these proteins from *B. napus* and its ortholog from *A. thaliana* that we named PARCL based on its functional and structural characteristics.

PARCL proteins bind RNAs and can act as RNA chaperones

The enrichment by heparin affinity chromatography and *in silico* analyses suggested that the highly abundant, formerly uncharacterized phloem protein PARCL might be an RBP, although no specific motif was found (Fig. 1). In addition to the protein, the endogenous PARCL transcript could be found in phloem samples, while other transcripts were absent (Fig. 2*A*). This is in good agreement with previous studies confirming the purity of phloem sap samples (21, 23). High affinities towards different RNAs in the low micromolar range could be experimentally determined by MST, independent of RNA size

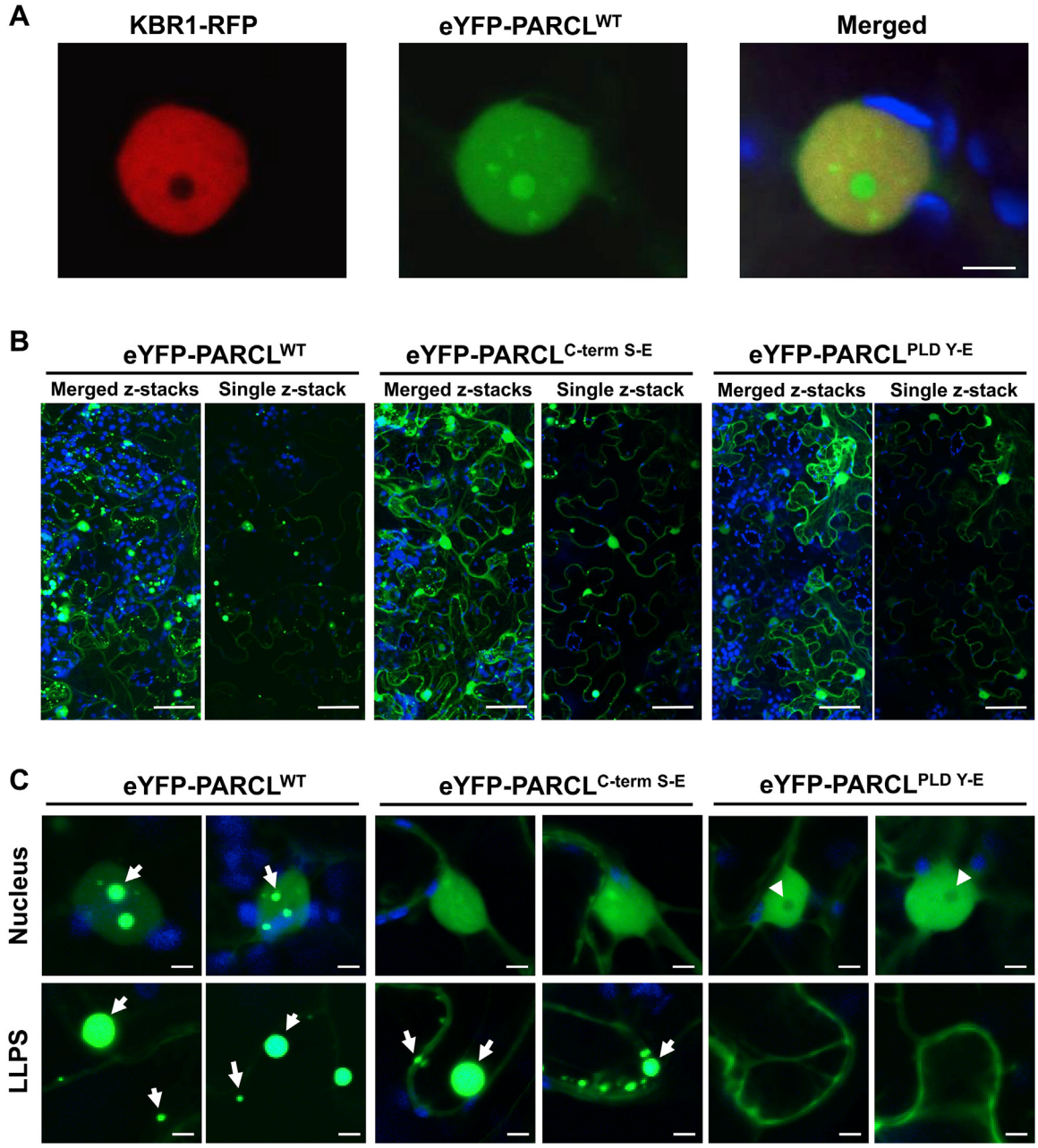

Figure 4. Confocal laser scanning microscopy images of eYFP-PARCL (*green*) localization in transiently expressing *Nicotiana benthamiana* leaves. *A*, three days after agroinfiltration, eYFP-PARCL appeared mainly in nuclei and nucleoli. Note that the coexpressed red fluorescent nuclear marker protein RFP-KBR1 showed a uniform nuclear distribution with no accumulation in nucleoli or puncta. Merged CLSM image shows eYFP-PARCL (*green*) and RFP-KBR1 (*red*), demonstrating the distinct nuclear distribution of eYFP-PARCL in coexpressing cells. *B* and *C*, comparison of different PARCL mutants on its localization in agroinfiltrated tobacco leaves. PARCL^{WT} appeared in nuclei, nucleoli, and as large condensates in the cytoplasm. Mutating the C-terminal S-rich region (PARCL$^{C\text{-term S-E}}$) to mimic phosphorylation reduced accumulation in nucleoli but did not affect cytosolic condensates. Mutating the PLD (PARCL$^{PLD\ S\text{-}E}$) by adding additional negative charges abolished nucleolar localization and cytosolic phase separation. *Blue*: plastid auto-fluorescence. *A* and *C*: Space bars represent 5 μm. B: Space bars represent 50 μm. CLSM, confocal laser scanning microscopy; PARCL, phloem-associated RNA chaperone-like; PLD, prion-like domain.

and without high preference for any RNA class (Fig. 2*B* and Table S3). However, only very low DNA affinity could be observed (Fig. S3*A* and Table S3). Possible explanations for the discrimination of DNA include specific recognition of ribose moieties or uracil (U) or detection of secondary RNA structures like hairpins, loops, or bulges. However, longer and highly structured tRNA and mRNA sequences were bound with affinities comparable to short and less structured miRNA sequences (Fig. 2*B* and Table S3), and sequences of equal length (miRNA and 21R-) exhibited large differences in affinities. These results suggest that ribose is not the binding target of PARCL. Also, the U base composition does not explain the differences in the affinities observed. The total content of uracil within the 21R- sequence was 33% compared to miR164 with 8%, while the binding affinity for 21R- was dramatically lower. Moreover, the antisense miR164 sequence

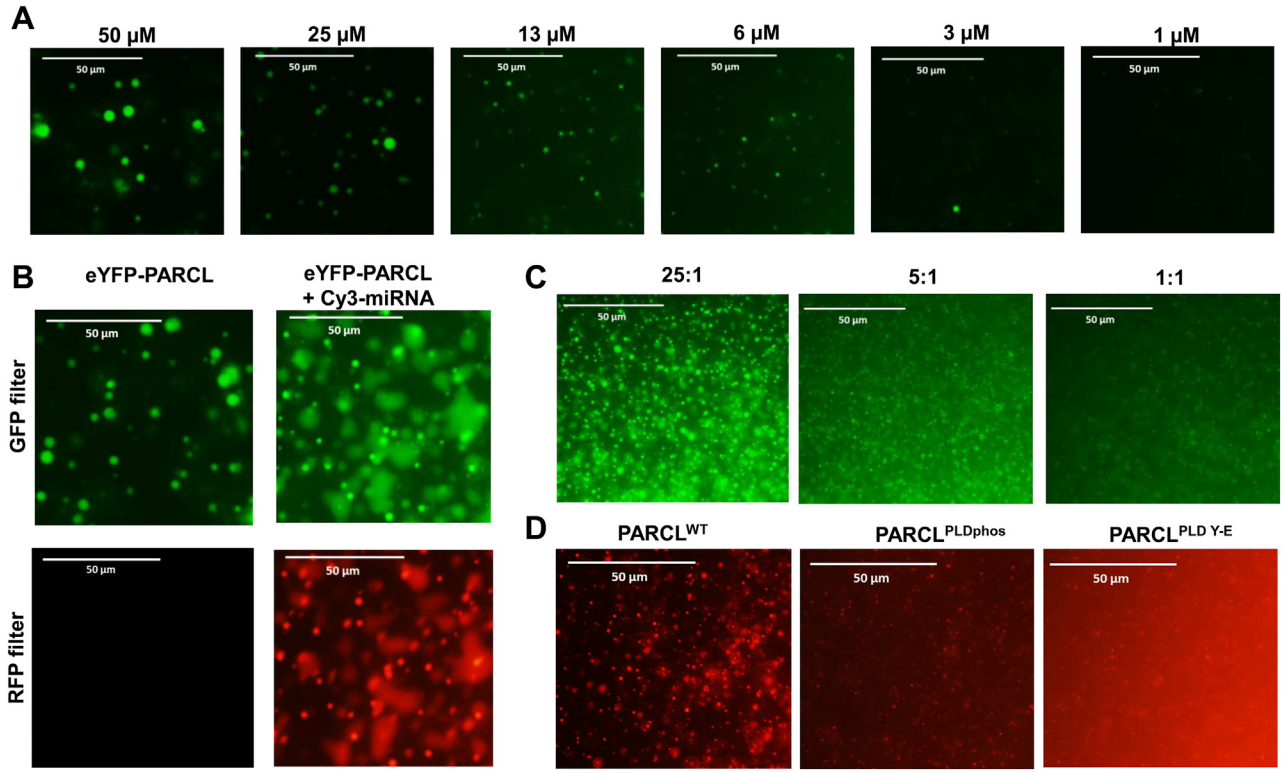

Figure 5. Phase separation assays of different PARCL constructs. *A*, concentration dependency of PARCL^{WT} on LLPS formation. The size of condensates increased with increasing protein concentration. *B*, incorporation of RNA into PARCL condensates. Fifty micromolar of eYFP-tagged PARCL was mixed with 1 μM of Cy3-labeled RNA (21R-). Cy3 was detected with a broadband RFP filter; eYFP was detected with a broadband GFP filter. Overlay of the signals show a complete colocalization, confirming the incorporation of RNA into PARCL condensates. *C*, impact of protein:RNA ratio on condensate size and density. At higher protein:RNA ratios (25:1), condensates showed a similar size and shape as PARCL without RNA. *Lower* ratios instead (5:1 and 1:1) decreased condensate size. *D*, effect of phosphorylation and tyrosine mutation on condensate formation. Ten micromolar of unphosphorylated PARCL was compared to 10 μM phosphorylated PARCL and PARCL$^{PLD\ Y\text{-}E}$. Tyrosine phosphorylation was achieved with FES kinase. Untagged PARCL was used and compared to untagged unphosphorylated and PARCL$^{PLD\ Y\text{-}E}$ proteins, since RNA can coseparate with PARCL, with Cy3 RNA for visualization. In contrast to the PARCL^{WT}, almost no condensates were visible in PARCL$^{PLD\ Y\text{-}E}$ and PARCL^{PLDphos}. PARCL, phloem-associated RNA chaperone-like; PLD, prion-like domain.

had a U content of 25% and PARCL proteins showed the same affinity towards both RNAs irrespective of their U base content. Similarly, ssRNAs and dsRNAs also showed no significant difference in binding (Fig. 2*B* and Table S3), suggesting that dsRNA or structured regions might not play a role in PARCL:RNA interaction. The reason why some RNAs showed at least 10-fold higher affinity than others, although the binding seems not to be sequence-specific, remains elusive.

PARCL also showed RNA strand annealing activity in chaperone assays (Fig. 3, *A* and *B*). The overall annealing rate of the two complementary RNAs was four times higher than background and similar to StpA, a protein known to facilitate RNA strand annealing (56, 57). A possible mechanism was postulated by Holmstrom *et al.* (66). PARCL as a highly positively charged molecule might act as a polyelectrolyte facilitating RNA folding, although selectivity towards RNA cannot be explained by this. High salt concentrations affected chaperone activity, strongly supporting the idea of a present polyelectrolyte (Fig. 3*C*). Common to such polyelectrolytes is their highly disordered nature. The increased RNA annealing rate induced by a pH shift (Fig. S6*B*) was initially thought to be caused by pH-induced structural rearrangements of the protein itself, but such changes could not be observed in SAXS measurements (Fig. S7*B*). Therefore, this increase might be due to stronger electrostatic interactions between RNA and protein, indicating a general mechanism of polyelectrolyte complexation. To corroborate that PARCL proteins are IDPs active in an unstructured state, PARCL was heat-denatured at 95 °C for 5 min and the chaperone assay was repeated. Heat denaturation did not affect annealing rates (Fig. S6*C*).

Several putative phosphorylation sites could be identified bioinformatically and PARCL has been found to be indeed phosphorylated (Figs. 1 and S5). *In vitro* phosphorylation assays with recombinant AtPARCL and BnPARCL confirmed that in addition to MAPK, CKII can phosphorylate the C-terminal S-segment (Fig. S5). This is in line with a previous report by Hoehenwarter *et al.* that identified AtPARCL as a target for protein phosphorylation (67). The predicted multiple phosphorylation sites might either influence protein localization or nucleic acid binding of the adjacent K-rich region (68–70). Consistent with the postulated loss of RNA-binding activity upon phosphorylation of serine-rich sequences (71, 72), phosphorylation of PARCL by CKII abolished this activity (Fig. 2*C*). It has been described previously that phosphorylation can promote RNA binding by influencing secondary structures of the RNA binding domains (8). However, phosphorylation in proximity or within binding regions can also reduce affinity (8, 73, 74). Serine phosphorylation of

PARCL could therefore function as a posttranslational switch for RNA binding and release. While a C-terminal phosphorylation strongly affected RNA binding and chaperone activity, it did not influence PARCL structural features (Figs. 2*C*, S6*D* and Table 1). In contrast to the C-terminal phosphorylation, a $PARCL^{PLD\ Y\text{-}E}$ mutation did not interfere with RNA binding (Fig. 2*C*), but could rather influence protein:protein interactions with itself and probably also other proteins as known for FUS and hnRNP2 (58, 59).

PARCL proteins are intrinsically disordered

SAXS measurements confirmed that the in-solution structure of PARCL was disordered, flexible (Fig. 3*D*) and not significantly affected by pH (Fig. S8). In contrast to compact and well folded globular proteins that have a distinct maximum in the dimensionless Kratky plot at $sR_g = \sqrt{3}$, the PARCL SAXS data exhibited no peak but instead formed a plateau that limits towards a value of 2 at $sR_g > 4$ that is typical of an IDP scattering profile (75). The resulting $p(r)$ profile (Table S4) as the summed-contribution of internal atom-pair distributions made from each individual conformer within the disordered PARCL population was rather skewed showing that the protein can sample compact-to-extended states. This 'ensemble anisotropy' is reflected in the spatially-aligned/minimized shape-volume of the ensemble obtained from *ab initio* bead modeling and the resulting volume-fraction weighted PARCL ensemble model representatives obtained from the ensemble optimization method (EOM; Fig. 3, *D* and *E*). The R_g distributions of the refined model pools calculated with EOM (χ^2 fit = 1.1–1.2; CorMap p = 0.05–0.16, Fig. S8) showed that relative to a random pool of structures, there is a slight bias toward a compact-sampling within the PARCL population, slightly more evident at pH 7.5. Although PARCL was structurally heterogeneous, as evidenced by the wide variance of the EOM R_g distributions, the protein did not appear as entirely random (Figs. 3, *D*, *E* and S8) but rather showed a distinct structural plasticity with probable implications for its RNA binding. Measuring stable RNA:protein complexes was impossible due to immediate precipitation.

CD spectroscopy confirmed a high degree of disorder of PARCL proteins under various conditions, independent of C-terminal phosphorylation or the addition of ligands (Table 1). Only SDS affected the overall folding of PARCL. Similar observations were made for other proteins harboring similar K-rich regions (70, 76, 77). It is believed that anionic detergents can induce class A2 amphipathic α-helices by binding the polar head groups to lysines. As a result, the induced shift from a more hydrated to a less hydrated environment can increase intramolecular hydrogen bonding of adjacent amino acid residues (78). Besides the K-rich region, also the putative PLD may induce a conformational change upon SDS binding as has been described for the disordered protein α-synuclein (79).

PARCL forms condensates in vitro *and* in vivo

The N-terminal repetitive motif [G/S]Y[G/S] of PARCL shows high similarity to the common prion-like motif and similar PLD motifs occur in all PARCL homologs. Generally, PLDs are found in several RBPs and are known to promote self-oligomerization that can be reversed by phosphorylation, arginine methylation, and other modifications (37, 58, 59, 80–83). PLD-containing proteins have been described to mediate protein phase separation, allowing the formation of membrane-less condensates to compartmentalize biomolecules, a mechanism of increasing interest also in plant biology (43–48). To determine PARCL localization and appearance *in vivo*, infiltration experiments in *N. benthamiana* with $PARCL^{WT}$ fused to eYFP were performed. Here, overexpressed PARCL occurred as large condensates in the cytosol and accumulated in nuclei and nucleoli (Fig. 4, *A* and *B*). This observation is in line with earlier studies describing that PLDs in RBPs are involved in the formation of RNA granules (84) and paranuclear speckles (37). $PARCL^{C\text{-}term\ S\text{-}E}$ showed less accumulation in nucleoli, but condensates were still visible. In contrast, the mutations in $PARCL^{PLD\ Y\text{-}E}$ reduced condensation and nucleolar localization dramatically (Fig. 4, *A*–*C*).

To characterize condensate formation in more detail, we performed additional *in vitro* phase separation experiments. Here, condensation could be induced under physiological conditions (10% PEG 3350, low salt, neutral pH) (Fig. 5). With increasing protein concentration, the size of condensates increased (Fig. 5*A*), what has already been shown for other PLD-containing proteins (85, 86). Next, fluorescently labeled small RNA was incubated with eYFP-$PARCL^{WT}$ and phase separation was imaged (Fig. 5*B*). Overlaying eYFP and Cy3 channel images confirmed that RNA was incorporated into the condensates. Noteworthy, RNA reshaped the appearance of the droplets, and the solution became more gel-like (Fig. 5*B*). Decreasing the protein:RNA ratio led to a reduction of condensate size (Fig. 5*C*), in line with previous studies showing that high RNA levels can inhibit phase separation while low RNA concentrations can promote it (64, 87).

Since condensation was abolished in the $PARCL^{PLD\ Y\text{-}E}$ mutant in *in vivo* experiments (Fig. 4), the effect on phase separation was analyzed *in vitro*. Because an effect of PLD phosphorylation on liquid-liquid phase separation LLPS has been described (58, 81), phosphorylated PARCL was included in the experiments. Since *in vitro* phosphorylation of eYFP-$PARCL^{WT}$ with the tyrosine kinases FES failed, we used unfused $PARCL^{WT}$ in the presence of labeled RNA for visualization. These experiments showed that tyrosine phosphorylation by FES had a similar effect as the $PARCL^{PLD\ Y\text{-}E}$ mutations. Noteworthy, DNA-dependent protein kinases like FES that are known to phosphorylate PLDs in other organisms are not existing in flowering plants like *A. thaliana* (88), suggesting that other so far unknown kinases might be involved. Both, $PARCL^{PLD\ Phos}$ and $PARCL^{PLD\ Y\text{-}E}$, did not entirely block phase separation but reduced the number of condensates considerably (Fig. 5*D*). This can be explained by an increased negative net charge within the PLD domain in both, the mutant and the phosphorylated PARCL, that could reduce the capacity for protein oligomerization. These results suggest that phosphorylation and other protein modifications altering the net charge of the PARCL PLD might act as a switch for reversible phase

separation. Similar observations were made in other organisms for RNA granule-forming proteins like Fus, hnRNP1/2, and other prion-like proteins (59, 89, 90). It was also shown in earlier studies that PLDs predominantly modulate protein granule formation by the interaction with tyrosines from other PLD-containing proteins (91) and are not involved in RNA binding (92–94). In contrast, our studies on the PARCL C-terminal S-rich region showed that RNA binding and chaperone activity were strongly reduced by phosphorylation (Figs. 2*C* and S6*D*) with no effect on condensate formation (Fig. 4, *B* and *C*). This is in agreement with studies showing that phosphorylation of the C-terminal S-rich region in other proteins might either influence protein localization or nucleic acid–binding capacity of the adjacent K-rich region (68–70). Taken together, our results suggest that PARCL possesses mechanisms to control protein:RNA interactions independent of protein:protein interactions with itself and probably also with other proteins.

Conclusions

In this study, we characterized one highly abundant phloem protein from *B. napus* and its ortholog from *A. thaliana* as a phloem-abundant, intrinsically disordered RBP with chaperone activity and high affinity towards a broad spectrum of RNAs. Moreover, PARCL proteins contain a PLD and form large condensates when transiently overexpressed in leaf infiltration experiments *in vivo*. *In vitro* phase separation studies suggest that the condensates are reversible and can incorporate RNA. Condensation can be regulated by modification of the net charge of the PLD, while RNA binding can be independently addressed by modification of the C-terminus. This would provide an elegant mechanism to control the formation of PARCL protein complexes independent of their RNA-binding activity, what could be important for RNA loading, transport, and unloading during long-distance transport.

Experimental procedures

Heparin affinity chromatography and protein identification

Phloem exudate from *B. napus* was collected from small incisions and purity control was performed as described previously (23, 50). To enrich putative nucleic acid–binding proteins, heparin affinity chromatography was performed using an ÄKTAprime plus (GE Healthcare). 1.5 ml of phloem exudate was diluted with 7.5 ml of buffer A (10 mM NaH_2PO_4 pH 7.0). After centrifugation (20.000*g*, 4 °C for 30 min), the supernatant was loaded onto a 1 ml heparin column (GE Healthcare) with a flow rate of 0.5 ml/min. The column was washed with 15 column volumes (CV) of buffer A supplemented with 0.5 M NaCl prior elution with an increasing NaCl concentration up to 2 M NaCl over 15 CV. One milliliter fractions were collected and proteins were precipitated as described previously (50). Proteins were resuspended in 25 µl SDS loading buffer and separated on a 12% SDS polyacrylamide gel by SDS-PAGE (Mini Protean III, Bio-Rad). For visualizing phosphorylated proteins, gels were stained with ProQ Diamond (Life Technologies) according to the manufacturer and subsequently stained with colloidal Coomassie (95). For protein identification, gel bands were excised and in-gel trypsin digested (21, 23, 96). The digests were loaded onto an AnchorChip and peptide mass fingerprint analysis was performed using a Bruker Ultraflex III MALDI-TOF/TOF (Bruker Daltonics GmbH) (see Table S1) and analyzed using mMass as published previously (23, 97).

In silico *analyses*

Amino acid composition and pI were calculated with the tool Protparam (ExPASy Proteomics server) (98). Sequence analyses were performed with homologous sequences from NCBI and Araport databases (Fig. S1). Motif recognition was achieved with the eukaryotic linear motif tool (99). Phosphorylation sites were predicted using NetPhos 3.1 with predictions for serine, threonine, and tyrosine phosphorylation (100). T-coffee was used for sequence alignment of PARCL orthologs from *the* Brassicaceae. RNA-binding prediction was performed with Pprint (101) with a threshold of 0.2. IUPred2 was used to calculate the overall degree of disorder (102).

Expression and purification of recombinant PARCL proteins

Full-length PARCL from *A. thaliana* Col-0 (At1g64370) and the homolog from *B. napus* (GenBank ID CDY46524) were amplified by PCR using Phusion High-Fidelity DNA Polymerase (Thermo Fisher Scientific) and sequence-specific oligonucleotides (Table S5) and cloned with and without an additional eYFP tag into the pET-28a vector (Novagen, Merck KGaA) using *Nde*I and *Xho*I as restriction enzymes (New England Biolabs). The constructs contained an N-terminal 6xHis-Tag and a thrombin cleavage site for tag removal. All plasmids were verified by DNA sequencing (Eurofins Genomics). The 6xHis-Tag-PARCL fusion proteins were expressed in *Escherichia coli* BL21 CodonPlus RIPL (DE3) cells (Agilent Technologies) by auto-induction (103). The cultures were incubated with 100 µg/ml kanamycin shaking at 170 rpm for at least 3 h at 37 °C and then transferred to 24 °C for overnight production. Cells were harvested by centrifugation and resuspended in buffer A (50 mM Tris–HCl pH 7.5 (at 4 °C), 300 mM NaCl) supplemented with 1 mg/ml lysozyme, 5 U/ml DNaseI, and 1 mM $MgCl_2$ and incubated for 1h at 4 °C followed by sonication (Branson Sonifier 250, Branson). After centrifugation at 43,000*g* for 30 min at 4 °C, the supernatant was filtrated through a 0.45 µm filter device and loaded onto a 5 ml HisTrap HP column (GE Healthcare) equilibrated with buffer A. The column was washed with 5 CV buffer B (50 mM Tris–HCl pH 7.5 (at 4 °C), 1 M NaCl, 20 mM imidazole) and eluted with buffer C (50 mM Tris–HCl (at 4 °C), 300 mM NaCl, 1 M imidazole) using a linear gradient over 25 CV from 0 to 1 M imidazole. Fractions containing the protein were pooled and supplemented with thrombin (GE Healthcare) according to the manufacturer protocol and dialyzed overnight against 50 mM Tris–HCl pH 7.5 (at 4 °C), 250 mM NaCl. A final purification to >95% purity was achieved by size-exclusion chromatography on a Superdex 75 (16/60) pg

column (GE Healthcare) run at 1 ml/min with 20 mM Tris–HCl pH 7.5 (at 4 °C), 200 mM NaCl. Purity was assayed by SDS-PAGE and colloidal Coomassie staining. The purified protein fractions were pooled again and concentrated up to 10 mg/ml using Vivaspin 20 (MWCO: 10 kD) centrifugal devices (Sartorius), frozen in liquid nitrogen, and stored in aliquots at −70 °C. For PARCL phosphorylation, the protein fraction after dialysis was treated with casein kinase II (CKII) (New England Biolabs) following the manufacturer's instructions at 30 °C for 2 h. PARCL was separated from CKII by gel filtration as described above.

RNA synthesis by in vitro *transcription with T7 RNA polymerase*

RNAs were synthesized by transcription of duplex DNA templates with T7 RNA polymerase (104). DNA templates for tRNAs were generated by PCR with Phusion High-Fidelity DNA Polymerase (Thermo Fisher Scientific) and a forward primer containing the T7 promotor sequence (5′-GGATC-TAATACGACTCACTATA-3′) according to manufacturer's instructions. miRNA templates were prepared by hybridizing sense and antisense DNA oligonucleotides (Table S7). Cy5-labeled RNA was obtained by overnight incubation of 10 pmol DNA template per 100 µl reaction, with 25 U/µl RNA polymerase, 0.005 U/µl inorganic pyrophosphatase supplemented with 2.5 mM ATP, 2.5 mM GTP, 2.5 mM CTP, 1 mM UTP, and 1 mM Cy5-UTP (Enzo Life Science) in transcription buffer (50 mM Hepes–NaOH pH 7.5, 15 mM $MgCl_2$, 5 mM DTT, 2 mM spermidine) at 37 °C. After removal of template DNA with 10 U of RNase-free DNaseI (Thermo Fisher Scientific) at 37 °C for 30 min and adding 5 µl of 500 mM EDTA to stop the reaction, transcripts were purified using the RNA Clean & Concentrator Kit 25 (Zymo Research) and confirmed by running a 2100 Bioanalyzer Nano chip (Agilent Technologies).

Microscale thermophoresis

To assay nucleic acid–protein interactions, MST experiments with a Monolith NT.115 (NanoTemper Technologies) were performed in at least triplicates using the standard protocol. A 16-step two-fold dilution series of protein was prepared, with the final concentration of protein ranging from 50 µM to 1.5 nM. The protein was mixed with 20 nM Cy5-labeled RNA in MST buffer (50 mM Tris–HCl pH 7.5 (at RT), 150 mM NaCl, 0.1% BSA, 0.05% Tween-20) and after incubation for 5 min at RT, the samples were loaded into Monolith NT.115 capillaries (NanoTemper Technologies) and subsequently subjected to MST analysis at 21 °C. Normalization and nonlinear curve fitting were done with Prism 5 (GraphPad Software) using the equation for a sigmoidal dose response. One-way ANOVA with miR164 as control was used for statistical analyses. Binding differences with $p < 0.05$ were regarded as significant.

RNA chaperone assays by FRET

RNA annealing assays were carried out according to Mayer *et al.* (56) (Fig. S6*A*). The 21-nt long complementary RNA-oligo 21R- (5′-Cy5-AUGUGGAAAAUCUCUAGCAGU-3′), was 5′ end labeled with Cy5, and the complementary 21R_rev (5′-Cy3-ACUGCUAGAGAUUUUCCACAU-3′) was 5′ end labeled with Cy3 (Eurofins Genomics). After injection of the two oligoribonucleotides (final concentration 10 nM) to annealing buffer (50 mM Hepes–NaOH pH 7.5, 3 mM $MgCl_2$, 1 mM DTT) alone or to annealing buffer with protein (final concentration 1 µM) with a final volume of 40 µl, the fluorescence of the fluorophores was measured with a Spark microplate reader (Tecan) at 37 °C for at least 180 s. The Cy3 donor fluorophore was excited at 535 nm once every 2 seconds and readings were collected at the two emission wavelengths 590 nm and 680 nm by switching between corresponding glass filters. The FRET index was calculated as the ratio of acceptor to donor dye fluorescence. Data were normalized and values were set at 1 after 5 min of measuring time to highlight differences in annealing velocities. Annealing velocities were calculated as described elsewhere (56, 57).

Size-exclusion chromatography SAXS and Size-exclusion chromatography with multi-angle laser light scattering

Size-exclusion chromatography coupled to small angle X-ray scattering measurements was performed at the EMBL P12 bioSAXS beam line at PETRA III (DESY) (105). Size-exclusion chromatography with multi-angle laser light scattering and refractive index measurements were performed using the same conditions and PARCL samples as described for SAXS. For more details on the experimental setup and data analysis, see supporting information methods (Methods S3).

In vivo *localization studies*

PARCL (At1g64370) cDNA was cloned from WT *A. thaliana* Col-0 plants in frame by Gateway recombination behind the 35S promoter–eYFP sequences of the pEarleygate 104 binary vector (106) or by genomic PCR *via* GW recombination with its predicted endogenous upstream promoter region of -483 bases and endogenous downstream terminator regions of 368 bases as a promoter eYFP - 6xAla (linker) - PARCL terminator fusion DNA into pMDC99. To analyze the subcellular distribution of eYFP-$PARCL^{WT}$, eYFP-$PARCL^{PLD\ Y\text{-}E}$, and eYFP-$PARCL^{C\text{-}term.\ S\text{-}E}$ fluorescent fusion protein, it was transiently coexpressed with the red fluorescent nuclear matrix marker fusion protein KBR1-RFP *via* agrobacterium (AGL1)–infiltration of *N. benthamiana* leaves (3–4 weeks after germination) or transformed into *A. thaliana* Col-0 WT as described (107). Two to four days after agrobacterium-infiltration, fusion protein localization was analyzed *via* confocal laser scanning microscopy (Leica SP8 spectral confocal laser scanning microscope, Leica Microsystems) in leaf epidermis cells. Infiltrated plant material and transgenic plant material was prepared with a razor blade and placed onto a microscope slide covered by an aqueous 10% glycerol solution. The excitation wavelength for YFP and RFP detection was

515 nm and 568 nm, respectively. Yellow fluorescence emission was detected at 525 to 580 nm, red fluorescence was detected at 610 to 630 nm, and chloroplast and cell wall autofluorescence were detected at 680 to 710 nm. For detection with multiple channels, scans were made sequentially to avoid false-positive signals caused by bleed-through.

Phase separation assay

To induce phase separation, different concentrations of PARCL were incubated with and without 1 μM or 10 μM Cy3-labeled 21R-RNA in phase separation buffer (50 mM Tris–HCl pH 7.5 at RT, 150 mM NaCl) for 10 min at room temperature. Subsequently, PEG3350 to a final concentration of 10% (w/v) was added and, after incubation for 15 min at RT, the samples were documented on an Olympus MVX10 Macroscope (Objective: MV Plapo 1× & 2×) equipped with a GFP and RFP filter system.

RT-PCR on B. napus *phloem sap*

The presence of the PARCL and pollen coat protein mRNAs were analyzed by RT-PCR as previously described (21, 23, 50). In brief, 150 ng of isolated phloem RNA were used for cDNA synthesis using the RevertAid RT reverse transcription kit (Thermo Fisher Scientific). Five microliters of synthesized cDNA were used for the subsequent RT-PCR. Pure phloem RNA will lead to a missing signal of the pollen coat protein transcript whereas a strong signal in flowers is anticipated.

Data availability

The final averaged SAXS profiles of PARCL and subsequent models are deposited in the Small Angle Scattering Biological Data Bank (SASBDB (108)) under the accession codes SASDJS7 (pH 7.5) and SASDJT7 (pH 6.5). The accession numbers for the sequences used in our phylogenetic analysis are given in Table S2.

Supporting information—This article contains supporting information.

Acknowledgments—We would like to thank Dana Schindelasch for excellent technical assistance and Frank Machin for his guidance and help in infiltration experiments.

Author contributions—A. O., S. O., R. J. M., F. K., and J. K. conceptualization; A. O., S. O., and J. K. methodology; A. O., S. O., S. F., C. M. J., D. I. S., C. B., and F. K. formal analysis; A. O., S. O., Y. Z., Z. C., L. W., K. R., L. v. P., S. F., C. M. J., D. I. S., C. B., and R. J. M. investigation; A. O., S. O., C. M. J., R. J. M., F. K., and J. K. writing–original draft; A. O., S. O., Y. Z., and C. M. J. visualization; Y. Z., Z. C., L. W., K. R., L. v. P., S. F., C. M. J., D. I. S., C. B., and F. K. writing–review and editing; S. F., D. I. S., C. B., F. K., and J. K. resources; S. F., C. M. J., and C. B. data curation; D. I. S., F. K., and J. K. validation; C. B., R. J. M., F. K., and J. K. funding acquisition; F. K. and J. K. supervision; J. K. project administration.

Funding and additional information—This work was financially supported by the European Research Council (ERC) Synergy grant ERCSyG 2018_810131 – PLAMORF awarded to R. J. M., F. K., and J. K. J. K. received further support by the ERC Career Integration Grant PCIG14-GA-2013-63 0734 and the Deutsche Forschungsgemeinschaft (DFG) grant DFG KE 856_6-1. C. M. J. and D. I. S. were further supported by iNEXT-Discovery, project number 871037, funded by the Horizon 2020 program of the European Commission. S. F. and C. B. acknowledge financial support by the Cluster of Excellence 'Advanced Imaging of Matter' of the Deutsche Forschungsgemeinschaft (DFG) - EXC 2056 - project ID 390715994.

Conflict of interest—The authors declare that they have no conflicts of interest with the contents of this article.

Abbreviations—The abbreviations used are: CV, column volume; EOMs, ensemble optimization method; IDP, intrinsically disordered protein; mRNA, messenger RNA; MST, Microscale thermophoresis; PARCL, phloem-associated RNA chaperone-like; PLD, prion-like domain; RBP, RNA-binding protein; RNP, ribonucleoprotein; SAXS, small angle X-ray scattering; tRNA, transfer RNA.

References

1. Jorgensen, R. A. (1998) An RNA-based information superhighway in plants. *Science* **279**, 1486–1487
2. Buhtz, A., Pieritz, J., Springer, F., and Kehr, J. (2010) Phloem small RNAs, nutrient stress responses, and systemic mobility. *BMC Plant Biol.* **10**, 64
3. Buhtz, A., Springer, F., Chappell, L., Baulcombe, D. C., and Kehr, J. (2008) Identification and characterization of small RNAs from the phloem of Brassica napus. *Plant J.* **53**, 739–749
4. Haywood, V., Yu, T.-S., Huang, N.-C., and Lucas, W. J. (2005) Phloem long-distance trafficking of GIBBERELLIC ACID-INSENSITIVE RNA regulates leaf development. *Plant J.* **42**, 49–68
5. Kim, M., Canio, W., Kessler, S., and Sinha, N. (2001) Developmental changes due to long-distance movement of a homeobox fusion transcript in tomato. *Science* **293**, 287–289
6. Thieme, C. J., Rojas-Triana, M., Stecyk, E., Schudoma, C., Zhang, W., Yang, L., *et al.* (2015) Endogenous Arabidopsis messenger RNAs transported to distant tissues. *Nat. Plants* **1**, 15025
7. Pant, B. D., Buhtz, A., and Kehr, J. (2008) MicroRNA399 is a long-distance signal for the regulation of plant phosphate homeostasis. *Plant J.* **53**, 731–738
8. Cho, S., Hoang, A., Sinha, R., Zhong, X.-Y., Fu, X.-D., Krainer, A. R., *et al.* (2011) Interaction between the RNA binding domains of Ser-Arg splicing factor 1 and U1-70K snRNP protein determines early spliceosome assembly. *Proc. Natl. Acad. Sci. U. S. A.* **108**, 8233–8238
9. Yoo, B.-C., Kragler, F., Varkonyi-Gasic, E., Haywood, V., Archer-Evans, S., Lee, Y. M., *et al.* (2004) A systemic small RNA signaling system in plants. *Plant Cell* **16**, 1979–2000
10. Zhang, S., Sun, L., and Kragler, F. (2009) The phloem-delivered RNA pool contains small noncoding RNAs and interferes with translation. *Plant Physiol.* **150**, 378–387
11. Ruiz-Medrano, R., Xoconostle-Cázares, B., and Lucas, W. J. (1999) Phloem long-distance transport of CmNACP mRNA: implications for supracellular regulation in plants. *Development* **126**, 4405–4419
12. Kehr, J., and Kragler, F. (2018) Long distance RNA movement. *New Phytol.* **218**, 29–40
13. Li, S., Wang, X., Xu, W., Liu, T., Cai, C., Chen, L., *et al.* (2021) Unidirectional movement of small RNAs from shoots to roots in interspecific heterografts. *Nat. Plants.* **7**, 50–59
14. Pant, B. D., Musialak-Lange, M., Nuc, P., May, P., Buhtz, A., Kehr, J., *et al.* (2009) Identification of nutrient-responsive Arabidopsis and rapeseed microRNAs by comprehensive real-time polymerase chain reaction profiling and small RNA sequencing. *Plant Physiol.* **150**, 1541–1555

15. Li, C., Gu, M., Shi, N., Zhang, H., Yang, X., Osman, T., *et al.* (2011) Mobile FT mRNA contributes to the systemic florigen signalling in floral induction. *Sci. Rep.* **1**, 73
16. Jaeger, K. E., and Wigge, P. A. (2007) FT protein acts as a long-range signal in Arabidopsis. *Curr. Biol.* **17**, 1050–1054
17. Corbesier, L., Vincent, C., Jang, S., Fornara, F., Fan, Q., Searle, I., *et al.* (2007) FT protein movement contributes to long-distance signaling in floral induction of Arabidopsis. *Science* **316**, 1030–1033
18. Banerjee, A. K., Lin, T., and Hannapel, D. J. (2009) Untranslated regions of a mobile transcript mediate RNA metabolism. *Plant Physiol.* **151**, 1831–1843
19. Branco, R., and Masle, J. (2019) Systemic signalling through translationally controlled tumour protein controls lateral root formation in Arabidopsis. *J. Exp. Bot.* **70**, 3927–3940
20. Berkowitz, O., Jost, R., Pollmann, S., and Masle, J. (2009) Characterization of TCTP, the translationally controlled tumor protein, from Arabidopsis thaliana. *Plant Cell* **20**, 3430–3447
21. Pahlow, S., Ostendorp, A., Krüßel, L., and Kehr, J. (2018) Phloem sap sampling from Brassica napus for 3D-PAGE of protein and ribonucleoprotein complexes. *J. Vis. Exp.* https://doi.org/10.3791/57097
22. Ham, B.-K., Brandom, J. L., Xoconostle-Cázares, B., Ringgold, V., Lough, T. J., and Lucas, W. J. (2009) A polypyrimidine tract binding protein, pumpkin RBP50, forms the basis of a phloem-mobile ribonucleoprotein complex. *Plant Cell* **21**, 197–215
23. Ostendorp, A., Pahlow, S., Krüßel, L., Hanhart, P., Garbe, M. Y., Deke, J., *et al.* (2017) Functional analysis of Brassica napus phloem protein and ribonucleoprotein complexes. *New Phytol.* **214**, 1188–1197
24. Zhang, W., Thieme, C. J., Kollwig, G., Apelt, F., Yang, L., Winter, N., *et al.* (2016) tRNA-related sequences trigger systemic mRNA transport in plants. *Plant Cell* **28**, 1237–1249
25. Yang, L., Perrera, V., Saplaoura, E., Apelt, F., Bahin, M., Kramdi, A., *et al.* (2019) m5C methylation guides systemic transport of messenger RNA over graft junctions in plants. *Curr. Biol.* **29**, 2465–2476.e5
26. Järvelin, A. I., Noerenberg, M., Davis, I., and Castello, A. (2016) The new (dis)order in RNA regulation. *Cell Commun. Signal.* **14**, 9
27. Re, A., Joshi, T., Kulberkyte, E., Morris, Q., and Workman, C. T. (2014) RNA–Protein interactions: an overview. In: Gorodkin, J., Ruzzo, W. L., eds.**, 1097**. *Methods in Molecular Biology*, Humana Press, Totowa, NJ: 491–521
28. Bellacosa, A., and Moss, E. G. (2003) RNA repair: damage control. *Curr. Biol.* **13**, R482–R484
29. Li, Z., Malla, S., Shin, B., and Li, J. M. (2014) Battle against RNA oxidation: molecular mechanisms for reducing oxidized RNA to protect cells. *Wiley Interdiscip. Rev. RNA.* **5**, 335–346
30. Lunde, B. M., Moore, C., and Varani, G. (2007) RNA-Binding proteins: modular design for efficient function. *Nat. Rev. Mol. Cell Biol.* **8**, 479–490
31. Hentze, M. W., Castello, A., Schwarzl, T., and Preiss, T. (2018) A brave new world of RNA-binding proteins. *Nat. Rev. Mol. Cell Biol.* **19**, 327–341
32. Castello, A., Fischer, B., Eichelbaum, K., Horos, R., Beckmann, B. M., Strein, C., *et al.* (2012) Insights into RNA biology from an atlas of mammalian mRNA-binding proteins. *Cell* **149**, 1393–1406
33. Van Roey, K., Gibson, T. J., and Davey, N. E. (2012) Motif switches: decision-making in cell regulation. *Curr. Opin. Struct. Biol.* **22**, 378–385
34. Lee, K., and Kang, H. (2016) Emerging roles of RNA-binding proteins in plant growth, development, and stress responses. *Mol. Cells.* **39**, 179–185
35. Jabeen, B., Naqvi, S. M. S., Mahmood, T., Sultana, T., Arif, M., and Khan, F. (2017) Ectopic expression of plant RNA chaperone offering multiple stress tolerance in E. coli. *Mol. Biotechnol.* **59**, 66–72
36. Woodson, S. A., Panja, S., and Santiago-Frangos, A. (2018) Proteins that chaperone RNA regulation. *Regul. RNA Bact. Archaea.* **6**, 383–397
37. Hennig, S., Kong, G., Mannen, T., Sadowska, A., Kobelke, S., Blythe, A., *et al.* (2015) Prion-like domains in RNA binding proteins are essential for building subnuclear paraspeckles. *J. Cell Biol.* **210**, 529–539
38. King, O. D., Gitler, A. D., and Shorter, J. (2012) The tip of the iceberg: RNA-binding proteins with prion-like domains in neurodegenerative disease. *Brain Res.* **1462**, 61–80
39. Paul, A., and Nancy, K. (2006) RNA granules. *J. Cell Biol.* **172**, 803–808
40. Vessey, J. P., Vaccani, A., Xie, Y., Dahm, R., Karra, D., Kiebler, M. A., *et al.* (2006) Dendritic localization of the translational repressor pumilio 2 and its contribution to dendritic stress granules. *J. Neurosci.* **26**, 6496–6508
41. Knowles, R. B., Sabry, J. H., Martone, M. E., Deerinck, T. J., Ellisman, M. H., Bassell, G. J., *et al.* (1996) Translocation of RNA granules in living neurons. *J. Neurosci.* **16**, 7812–7820
42. Kiebler, M. A., and Bassell, G. J. (2006) Neuronal RNA granules: movers and makers. *Neuron* **51**, 685–690
43. Chakrabortee, S., Kayatekin, C., Newby, G. A., Mendillo, M. L., Lancaster, A., and Lindquist, S. (2016) Luminidependens (LD) is an Arabidopsis protein with prion behavior. *Proc. Natl. Acad. Sci. U. S. A.* **113**, 6065–6070
44. Dorone, Y., Boeynaems, S., Flores, E., Jin, B., Hateley, S., Bossi, F., *et al.* (2021) A prion-like protein regulator of seed germination undergoes hydration-dependent phase separation. *Cell* **184**, 4284–4298.e27
45. Fang, X., Wang, L., Ishikawa, R., Li, Y., Fiedler, M., Liu, F., *et al.* (2019) Arabidopsis FLL2 promotes liquid–liquid phase separation of polyadenylation complexes. *Nature* **569**, 265–269
46. Powers, S. K., Holehouse, A. S., Korasick, D. A., Schreiber, K. H., Clark, N. M., Jing, H., *et al.* (2019) Nucleo-cytoplasmic partitioning of ARF proteins controls auxin responses in Arabidopsis thaliana. *Mol. Cell.* **76**, 177–190.e5
47. van Dop, M., Fiedler, M., Mutte, S., de Keijzer, J., Olijslager, L., Albrecht, C., *et al.* (2020) DIX domain polymerization drives assembly of plant cell polarity complexes. *Cell* **180**, 427–439.e12
48. Zhang, Y., Li, Z., Chen, N., Huang, Y., and Huang, S. (2020) Phase separation of Arabidopsis EMB1579 controls transcription, mRNA splicing, and development. *PLoS Biol.* **18**, e3000782
49. Anstead, J. A., Hartson, S. D., and Thompson, G. A. (2013) The broccoli (Brassica oleracea) phloem tissue proteome. *BMC Genomics* **14**, 764
50. Giavalisco, P., Kapitza, K., Kolasa, A., Buhtz, A., and Kehr, J. (2006) Towards the proteome of Brassica napus phloem sap. *Proteomics* **6**, 896–909
51. Lin, M.-K., Lee, Y.-J., Lough, T. J., Phinney, B. S., and Lucas, W. J. (2009) Analysis of the pumpkin phloem proteome provides insights into angiosperm sieve tube function. *Mol. Cell. Proteomics* **8**, 343–356
52. Lattanzio, G., Andaluz, S., Matros, A., Calvete, J. J., Kehr, J., and Abadía, J. (2013) Protein profile of lupinus texensis phloem sap exudates: searching for Fe and Zn containing proteins. *Proteomics* **13**, 2283–2296
53. Bolten, S. N., Rinas, U., and Scheper, T. (2018) Heparin: role in protein purification and substitution with animal-component free material. *Appl. Microbiol. Biotechnol.* **102**, 8647–8660
54. Nickelsen, J., and Link, G. (1993) The 54 kDa RNA-binding protein from mustard chloroplasts mediates endonucleolytic transcript 3′ end formation *in vitro*. *Plant J.* **3**, 537–544
55. Genersch, E., Eckerskorn, C., Lottspeich, F., Herzog, C., Kühn, K., and Pöschl, E. (1995) Purification of the sequence-specific transcription factor CTCBF, involved in the control of human collagen IV genes: subunits with homology to Ku antigen. *EMBO J.* **14**, 791–800
56. Mayer, O., Rajkowitsch, L., Lorenz, C., Konrat, R., and Schroeder, R. (2007) RNA chaperone activity and RNA-binding properties of the E. coli protein StpA. *Nucl. Acids Res.* **35**, 1257–1269
57. Rajkowitsch, L., and Schroeder, R. (2007) Coupling RNA annealing and strand displacement: a FRET-based microplate reader assay for RNA chaperone activity. *Biotechniques* **43**, 304–310
58. Ryan, V. H., Perdikari, T. M., Naik, M. T., Saueressig, C. F., Lins, J., Dignon, G. L., *et al.* (2021) Tyrosine phosphorylation regulates hnRNPA2 granule protein partitioning and reduces neurodegeneration. *EMBO J.* **40**, e105001
59. Monahan, Z., Ryan, V. H., Janke, A. M., Burke, K. A., Rhoads, S. N., Zerze, G. H., *et al.* (2017) Phosphorylation of the FUS low-complexity domain disrupts phase separation, aggregation, and toxicity. *EMBO J.* **36**, 2951–2967
60. Chen, Y., and Varani, G. (2005) Protein families and RNA recognition. *FEBS J.* **272**, 2088–2097

61. Henderson, B. R., and Kühn, L. C. (1997) Interaction between iron-regulatory proteins and their RNA target sequences, iron-responsive elements. *Prog. Mol. Subcell. Biol.* **18**, 117–139
62. Forman-Kay, J. D., Ditlev, J. A., Nosella, M. L., and Lee, H. O. (2022) What are the distinguishing features and size requirements of biomolecular condensates and their implications for RNA-containing condensates? *RNA* **28**, 36–47
63. Matheny, T., Van Treeck, B., Huynh, T. N., and Parker, R. (2021) RNA partitioning into stress granules is based on the summation of multiple interactions. *RNA* **27**, 174–189
64. Alshareedah, I., Moosa, M. M., Raju, M., Potoyan, D. A., and Banerjee, P. R. (2020) Phase transition of RNA–protein complexes into ordered hollow condensates. *Proc. Natl. Acad. Sci. U. S. A.* **117**, 15650–15658
65. Guo, Q., Shi, X., and Wang, X. (2021) RNA and liquid-liquid phase separation. *Non-coding RNA Res.* **6**, 92–99
66. Holmstrom, E. D., Liu, Z., Nettels, D., Best, R. B., and Schuler, B. (2019) Disordered RNA chaperones can enhance nucleic acid folding *via* local charge screening. *Nat. Commun.* **10**, 2453
67. Hoehenwarter, W., Thomas, M., Nukarinen, E., Egelhofer, V., Röhrig, H., Weckwerth, W., *et al.* (2013) Identification of novel *in vivo* MAP kinase substrates in Arabidopsis thaliana through use of tandem metal oxide affinity chromatography. *Mol. Cell. Proteomics* **12**, 369–380
68. Goday, A., Jensen, A. B., Culiáñez-Macià, F. A., Mar Albà, M., Figueras, M., Serratosa, J., *et al.* (1994) The maize abscisic acid-responsive protein Rab17 is located in the nucleus and interacts with nuclear localization signals. *Plant Cell* **6**, 351–360
69. Lange, A., McLane, L. M., Mills, R. E., Devine, S. E., and Corbett, A. H. (2010) Expanding the definition of the classical bipartite nuclear localization signal. *Traffic* **11**, 311–323
70. Graether, S. P., and Boddington, K. F. (2014) Disorder and function: a review of the dehydrin protein family. *Front. Plant Sci.* **5**, 576
71. García-Mauriño, S. M., Rivero-Rodríguez, F., Velázquez-Cruz, A., Hernández-Vellisca, M., Díaz-Quintana, A., la Rosa, M. A., *et al.* (2017) RNA binding protein regulation and cross-talk in the control of AU-rich mRNA fate. *Front. Mol. Biosci.* **4**, 71
72. Corley, M., Burns, M. C., and Yeo, G. W. (2020) How RNA-binding proteins interact with RNA: molecules and mechanisms. *Mol. Cell.* **78**, 9–29
73. Kuehnert, J., Sommer, G., Zierk, A. W., Fedarovich, A., Brock, A., Fedarovich, D., *et al.* (2015) Novel RNA chaperone domain of RNA-binding protein La is regulated by AKT phosphorylation. *Nucl. Acids Res.* **43**, 581–594
74. Thapar, R. (2015) Structural basis for regulation of RNA-binding proteins by phosphorylation. *ACS Chem. Biol.* **10**, 652–666
75. Receveur-Brechot, V., and Durand, D. (2012) How random are intrinsically disordered proteins? a small angle scattering perspective. *Curr. Protein Pept. Sci.* **13**, 55–75
76. Koag, M.-C., Fenton, R. D., Wilkens, S., and Close, T. J. (2003) The binding of maize DHN1 to lipid vesicles. Gain of structure and lipid specificity. *Plant Physiol.* **131**, 309–316
77. Koag, M.-C., Wilkens, S., Fenton, R. D., Resnik, J., Vo, E., and Close, T. J. (2009) The K-segment of maize DHN1 mediates binding to anionic phospholipid vesicles and concomitant structural changes. *Plant Physiol.* **150**, 1503–1514
78. Pessarakli, M. (2019). CRC Press. In *Handbook of Plant and Crop Stress*, Fourth edition, CRC Press, Taylor & Francis Group, Boca Raton, FL
79. Takaramoto, S., Nakasone, Y., Sadakane, K., Maruta, S., and Terazima, M. (2021) Time-resolved detection of SDS-induced conformational changes in α-synuclein by a micro-stopped-flow system. *RSC Adv.* **11**, 1086–1097
80. Yang, L., Gal, J., Chen, J., and Zhu, H. (2014) Self-assembled FUS binds active chromatin and regulates gene transcription. *Proc. Natl. Acad. Sci. U. S. A.* **111**, 17809–17814
81. Luo, Y.-Y., Wu, J.-J., and Li, Y.-M. (2021) Regulation of liquid–liquid phase separation with focus on post-translational modifications. *Chem. Commun.* **57**, 13275–13287
82. Hofweber, M., Hutten, S., Bourgeois, B., Spreitzer, E., Niedner-Boblenz, A., Schifferer, M., *et al.* (2018) Phase separation of FUS is suppressed by its nuclear import receptor and arginine methylation. *Cell* **173**, 706–719.e13
83. Qamar, S., Wang, G., Randle, S. J., Ruggeri, F. S., Varela, J. A., Lin, J. Q., *et al.* (2018) FUS phase separation is modulated by a molecular chaperone and methylation of arginine cation-π interactions. *Cell* **173**, 720–734.e15
84. Boncella, A. E., Shattuck, J. E., Cascarina, S. M., Paul, K. R., Baer, M. H., Fomicheva, A., *et al.* (2020) Composition-based prediction and rational manipulation of prion-like domain recruitment to stress granules. *Proc. Natl. Acad. Sci. U. S. A.* **117**, 5826–5835
85. Alberti, S. (2017) Phase separation in biology. *Curr. Biol.* **27**, R1097–R1102
86. Patel, A., Lee, H. O., Jawerth, L., Maharana, S., Jahnel, M., Hein, M. Y., *et al.* (2015) A liquid-to-solid phase transition of the ALS protein FUS accelerated by disease mutation. *Cell* **162**, 1066–1077
87. Maharana, S., Wang, J., Papadopoulos, D. K., Richter, D., Pozniakovsky, A., Poser, I., *et al.* (2018) RNA buffers the phase separation behavior of prion-like RNA binding proteins. *Science* **360**, 918–921
88. Lees-Miller, J. P., Cobban, A., Katsonis, P., Bacolla, A., Tsutakawa, S. E., Hammel, M., *et al.* (2021) Uncovering DNA-PKcs ancient phylogeny, unique sequence motifs and insights for human disease. *Prog. Biophys. Mol. Biol.* **163**, 87–108
89. Monahan, Z. T., Rhoads, S. N., Yee, D. S., and Shewmaker, F. P. (2018) Yeast models of prion-like proteins that cause amyotrophic lateral sclerosis reveal pathogenic mechanisms. *Front. Mol. Neurosci.* **11**, 1–11
90. Molliex, A., Temirov, J., Lee, J., Coughlin, M., Kanagaraj, A. P., Kim, H. J., *et al.* (2015) Phase separation by low complexity domains promotes stress granule assembly and drives pathological fibrillization. *Cell* **163**, 123–133
91. Wang, J., Choi, J.-M., Holehouse, A. S., Lee, H. O., Zhang, X., Jahnel, M., *et al.* (2018) A molecular grammar governing the driving forces for phase separation of prion-like RNA binding proteins. *Cell* **174**, 688–699.e16
92. Riback, J. A., Katanski, C. D., Kear-Scott, J. L., Pilipenko, E. V., Rojek, A. E., Sosnick, T. R., *et al.* (2017) Stress-triggered phase separation is an adaptive, evolutionarily tuned response. *Cell* **168**, 1028–1040.e19
93. Franzmann, T. M., and Alberti, S. (2019) Prion-like low-complexity sequences: key regulators of protein solubility and phase behavior. *J. Biol. Chem.* **294**, 7128–7136
94. Burke, K. A., Janke, A. M., Rhine, C. L., and Fawzi, N. L. (2015) Residue-by-Residue view of *in vitro* FUS granules that bind the C-terminal domain of RNA polymerase II. *Mol. Cell* **60**, 231–241
95. Dyballa, N., and Metzger, S. (2009) Fast and sensitive colloidal coomassie G-250 staining for proteins in polyacrylamide gels. *J. Vis. Exp.* https://doi.org/10.3791/1431
96. Walz, C., Juenger, M., Schad, M., and Kehr, J. (2002) Evidence for the presence and activity of a complete antioxidant defence system in mature sieve tubes. *Plant J.* **31**, 189–197
97. Strohalm, M., Hassman, M., Kosata, B., and Kodícek, M. (2008) mMass data miner: an open source alternative for mass spectrometric data analysis. *Rapid Commun. Mass Spectrom.* **22**, 905–908
98. Gasteiger, E., Hoogland, C., Gattiker, A., Duvaud, S., Wilkins, M. R., Appel, R. D., *et al.* (2005). In: Walker, J. M., ed. *The Proteomics Protocols Handbook*, Humana Press, Totowa, NJ. https://doi.org/10.1385/1592598900
99. Kumar, M., Gouw, M., Michael, S., Sámano-Sánchez, H., Pancsa, R., Glavina, J., *et al.* (2020) ELM-the eukaryotic linear motif resource in 2020. *Nucl. Acids Res.* **48**, D296–D306
100. Blom, N., Sicheritz-Pontén, T., Gupta, R., Gammeltoft, S., and Brunak, S. (2004) Prediction of post-translational glycosylation and phosphorylation of proteins from the amino acid sequence. *Proteomics* **4**, 1633–1649
101. Kumar, M., Gromiha, M. M., and Raghava, G. P. S. (2008) Prediction of RNA binding sites in a protein using SVM and PSSM profile. *Proteins* **71**, 189–194
102. Mészáros, B., Erdős, G., and Dosztányi, Z. (2018) IUPred2A: Context-dependent prediction of protein disorder as a function of redox state and protein binding. *Nucl. Acids Res.* **46**, W329–W337

103. Studier, F. W. (2005) Protein production by auto-induction in high-density shaking cultures. *Protein Expr. Purif.* **41**, 207–234
104. Cazenave, C., and Uhlenbeck, O. C. (1994) RNA template-directed RNA synthesis by T7 RNA polymerase. *Proc. Natl. Acad. Sci. U. S. A.* **91**, 6972–6976
105. Blanchet, C. E., Spilotros, A., Schwemmer, F., Graewert, M. A., Kikhney, A., Jeffries, C. M., *et al.* (2015) Versatile sample environments and automation for biological solution X-ray scattering experiments at the P12 beamline (PETRA III, DESY). *J. Appl. Crystallogr.* **48**, 431–443
106. Earley, K. W., Haag, J. R., Pontes, O., Opper, K., Juehne, T., Song, K., *et al.* (2006) Gateway-compatible vectors for plant functional genomics and proteomics. *Plant J.* **45**, 616–629
107. Winter, N., Kollwig, G., Zhang, S., and Kragler, F. (2007) MPB2C, a microtubule-associated protein, regulates non-cell-autonomy of the homeodomain protein KNOTTED1. *Plant Cell* **19**, 3001–3018
108. Valentini, E., Kikhney, A. G., Previtali, G., Jeffries, C. M., and Svergun, D. I. (2015) SASBDB, a repository for biological small-angle scattering data. *Nucl. Acids Res.* **43**, D357–D363